Synthesis and Magnetic Properties of Ferrimagnetic CoFe$_2$O$_4$ Nanoparticles Embedded in an Antiferromagnetic NiO Matrix

Mathieu Artus,[†] Souad Ammar,*,[†] Lorette Sicard,[†] Jean-Yves Piquemal,[†] Frédéric Herbst,[†] Marie-Joseph Vaulay,[†] Fernand Fiévet,[†] and Vincent Richard[‡]

ITODYS, Université Paris 7, UMR-CNRS 7086, 2 Place Jussieu, 75251 Paris, France, and LRS, Université Paris 6, UMR-CNRS 7609, 4 Place Jussieu, 75252 Paris, France

Received August 29, 2007. Revised Manuscript Received May 5, 2008

Ultrafine cobalt ferrite nanoparticles were prepared by forced hydrolysis in diethyleneglycol and, after centrifugation, dispersed in the same solvent to form a sol in which a layered hydroxyacetate nickel salt was precipitated. The as-obtained composite was moderately calcined in air to form nanoparticles constituted by a ferrimagnetic CoFe$_2$O$_4$ core embedded in well-crystallized antiferromagnetic NiO. Magnetic properties such as coercivity, hysteresis loop shift, and blocking temperature were analyzed regarding exchange bias features by comparing the magnetic data measured on these particles to those obtained on fresh CoFe$_2$O$_4$ particles mechanically dispersed in a diamagnetic Al$_2$O$_3$ matrix.

Introduction

Because of their very small size, nanoparticles display peculiar magnetic properties that differ from those of bulk materials. The variety of potential applications, particularly for reversible and irreversible ultrahigh-density information storage, has stimulated the interest of a large portion of the scientific community. However, the finite size of the particles induces superparamagnetic behavior at room temperature, which is a drawback for magnetic recording applications. Indeed, the blocking temperature, T_B, which measures the thermal transition from the blocked ferro- or ferrimagnetic state to the superparamagnetic one, is usually lower than 300 K. Consequently, the recording units become thermally unstable at the operating temperature. Nevertheless, T_B depends not only on the size but also on the magnetic anisotropy energy of the nanoparticles. T_B can thus be increased by raising this last parameter. The anisotropy energy is mainly driven by the structure and microstructure of the particles.[1–3] In recent years, a supplementary anisotropy term was evidenced in nanostructures consisting of a ferro- or ferrimagnetic core embedded in an antiferromagnet. It is called exchange bias, and it is due to exchange coupling between the spins at the interface between the ferromagnetic core and the antiferromagnetic shell. The interfacial magnetic structure is affected by competition between the different magnetic orderings. Especially, it may induce unidirectional anisotropy in the core, below the Néel temperature (T_N) of the shell, causing a shift in the hysteresis loop when the material is cooled in the presence of an applied field from a starting temperature between T_N and Curie temperature (T_C)

of the magnetic core.[4] This additional anisotropy can increase considerably the T_B value and then beat the superparamagnetic limit. Such behavior was reported for a wide variety of materials: Co/CoO,[4–6] NiCo/NiCoO,[7] Cr$_2$O$_3$/CrO$_2$,[8] FePt/Fe$_3$O$_4$,[9] Fe$_3$O$_4$/FeO,[10,11] etc.

The fabrication strategy for such materials is still in a primitive stage. The first synthesis method described consisted of chemically modifying the surface of a preformed ferro- or ferrimagnetic core. Very often, a metallic ferromagnetic core produced by physical methods is oxygen passivated, and the resulting native oxide constitutes the antiferromagnetic shell. This is, for instance, the case in the Fe/FeO$_x$[12] system. Chemical surface modification also could result from prolonged N$_2$ or H$_2$S gas exposition at high temperatures to form an antiferromagnetic nitride or sulfide shell on preformed ferromagnetic metal nanoparticles. This is the case, for instance, in the Co/CoN[13] or Fe/FeS[14] systems. In every case, this method is very restrictive. The number of systems in which an exchange bias could be observed is rather limited because this experimental approach does not always allow the production of various heterogeneous magnetic materials with a controlled composition and structure.

* Corresponding author. E-mail: ammarmer@univ-paris-diderot.fr.
  † Université Paris 7.
  ‡ Université Paris 6.

(1) Kodama, R. H. *J. Magn. Magn. Mater.* **1999,** *200,* 359.
(2) Kremenovic, A.; Antic, B.; Spasojevic, V.; Vucinic-Vasic, M.; Jaglicic, Z.; Pirnat, J.; Trontelj, Z. *J. Phys.: Condens. Matter* **2005,** *17,* 4285.
(3) Vestal, C. R.; Song, Q.; Zhang, Z. J. *J. Phys. Chem. B* **2004,** *108,* 18222.
(4) Skumryev, V.; Stoyanov, S.; Zhang, Y.; Hadjipanayis, G.; Givord, D.; Nogués, N. *Nature (London, U.K.)* **2003,** *423,* 850.
(5) Wiedwad, U.; Lindner, J.; Spasova, M.; Frait, Z.; Farle, M. *Phase Trans.* **2005,** *78,* 85.
(6) Koch, S. A.; Palasantzas, G.; Vystavel, T.; Hosson, J. T. M. D.; Binns, C.; Looch, S. *Phys. Rev. B: Condens. Matter Mater. Phys.* **2005,** *71,* 85410.
(7) Jeyadevan, B.; Chinnasamy, C. N.; Perales-Perez, O.; Iwasaki, Y.; Hobo, A.; Shinoda, K.; Tohji, K.; Kasuya, A. *IEEE Trans. Magn.* **2002,** *38,* 2595.
(8) Zheng, R. K.; Liu, H.; Wang, Y.; Zhang, X. X. *Appl. Phys. Lett.* **2004,** *84,* 702.
(9) Zeng, H.; Li, J.; Wang, Z. L.; Liu, J. P.; Sun, S. *Nano Lett.* **2004,** *4,* 187.
(10) Das, D.; Roya, S.; Chen, J. W.; Chakravorty, D. *J. Appl. Phys.* **2002,** *91,* 4573.
(11) Del Bianco, L.; Fiorani, D.; Testa, A. M.; Bonetti, E. *Phys. Rev. B: Condens. Matter Mater. Phys.* **2005,** *290–291,* 102.

The second method to form ferromagnetic/antiferromagnetic core/shell nanostructures is based on ball milling. It consists of mixing high-purity ferro- or ferrimagnetic and antiferromagnetic powders in different weight ratios under an argon atmosphere (see, i.e., the preparation of Co/NiO or Co/FeS systems[15]). This route is very versatile and could permit the preparation of a large variety of materials, but it does not offer real control of the morphology within a characteristic dimension lying in the nanometer range for the produced particles.

The third method is based on the physical vapor deposition of an antiferromagnetic shell or its chemical precipitation on preformed ferro- or ferrimagnetic nanoparticles. This is, for instance, the case in the fabrication of CrO_2/Cr_2O_3 core/shell nanoparticles, where commercial CrO_2 particles were enclosed in an epitaxial 2.5 nm thickened Cr_2O_3 layer,[16] or in the fabrication of spinel ferrite/MnO core/shell nanoparticles.[17] In this last example, the ferrite particles, such as $CoFe_2O_4$ or $ZnFe_2O_4$, were previously produced via high-temperature (~573 K) decomposition of acetylacetonate metal complexes in benzyl ether in the presence of 1,2-hexadecanediol and capping agents. They were then coated by MnO via seed-mediated growth in hexane using manganese acetate salts. This method is very interesting since it offers both a better morphological control and a wide variety of inorganic coating, but, at this moment, it is mainly dedicated to the fabrication of oxide/oxide nanostructures. As an alternative to this method, we propose in the present work to prepare such nanostructures by an easy, reproducible, and relatively low-temperature chemical route, namely, the polyol method. The polyol process is a very efficient and versatile chimie douce route. Polyols act as amphiprotic solvents, as well as complexing, reducing, and surfactant agents. They permit the production of monodisperse metal,[18] oxide,[19−21] or sulfide[22] nanoparticles and different transition metal layered hydroxide salts.[23,24] They also offer the opportunity of incorporating the interslabs or adsorbing on the crystallites of these lamellar compounds variable quantities of preformed nanoparticles.[25] Moreover, the dehydroxylation of such hydroxide phases leads to the formation of their corresponding oxides, which are often antiferromagnetic, opening thus true opportunities in the fabrication of various ferro- or ferrimagnetic nanoparticles embedded in an antiferromagnet. We demonstrate, for the first time, the possibility of fabricating nanostructures almost uniform in shape and size exhibiting bias exchange by the so-called polyol process. It consists of the precipitation of a layered hydroxyacetate nickel salt $Ni(OH)_{1.6}(CH_3CO_2)_{0.4} \cdot nH_2O$ (LHS) in a polyol solution containing preformed monodisperse cobalt ferrite nanoparticles, followed by moderate calcination to dehydroxylate the LHS phase into a nickel oxide one, to form nanoparticles constituted by a ferrimagnetic $CoFe_2O_4$ core embedded in an antiferromagnetic NiO matrix.

This work aims at studying the improvement of the thermal magnetic stability of very small ferrimagnetic $CoFe_2O_4$ nanoparticles embedded in an antiferromagnetic NiO matrix, produced as described previously, with respect to the properties of the same $CoFe_2O_4$ particles dispersed in a diamagnetic Al_2O_3 matrix, prepared by simple mechanical mixing. We fixed the particle concentration in these matrices at ~3−4 wt %. The mass concentration of $CoFe_2O_4$ in the final composites was voluntarily chosen to be lower than required for many applications (i.e., magnetic storage) to reduce dipolar interparticle effects. Indeed, such interactions can affect greatly the magnetic behavior of superparamagnets. They can modulate the coercivity as well as the blocking temperature. An optimization of the NiO/$CoFe_2O_4$ composite for specific applications is required here.

Experimental Procedures

Synthesis. Metal acetates $Ni(CH_3COO)_2 \cdot 4H_2O$, $Co(CH_3COO)_2 \cdot 4H_2O$, $Fe(CH_3COO)_2$, and diethyleneglycol (DEG) were purchased from Acros. Alumina Al_2O_3 was purchased from Kaiser. All products were used without any further purification.

The $CoFe_2O_4$ nanoparticles were obtained by forced hydrolysis in a polyol medium.[26] A total of 0.435 g (2.5 mmol) of $Fe(CH_3COO)_2$ and 0.311 g (1.25 mmol) of $Co(CH_3COO)_2 \cdot 4H_2O$ was dissolved in 250 mL of DEG. The mixture was heated up to the boiling point (510 K) for 1 h under mechanical stirring. It was then cooled to room temperature, and the centrifuged product was washed 3 times with ethanol. Ten milligrams of the separated particles was dispersed by sonification in 200 mL of DEG to prepare a slightly brown sol. This sol and 82.5 mL of distilled water were added to a solution of 4.66 g (18.75 mmol) of $Ni(CH_3COO)_2 \cdot 4H_2O$ dissolved in 50 mL of DEG, to obtain a nominal Co/Ni atomic ratio of 0.0023. The mixture was heated at 335 K for 18 h to form a layered hydroxide salt of nickel (LHS)[27] in the presence of cobalt ferrite nanoparticles. At the end of the reaction, fast cooling was needed to avoid rapid dissolution of the LHS phase. The final product was centrifuged and washed several times with ethanol. Finally, the blend of $CoFe_2O_4$ and nickel LHS was heated at 573 K for 24 h under air flow, to dehydroxylate the LSH into NiO. All the precursor nominal concentrations in the fabrication of the LHS/$CoFe_2O_4$ and then NiO/$CoFe_2O_4$ composites were chosen according to the sol stability of the ferrite nanoparticles in the mixed DEG and water solvent.

(12) Prados, C.; Multigner, M.; Hernando, A.; Sanchez, J. C.; Fernandez, A.; Conde, C. F.; Conde, A. *J. Appl. Phys.* **1999**, *85*, 6118.

(13) Lin, H. M.; Hsu, C. M.; Yao, Y. D.; Chen, Y. Y.; Kuan, T. T.; Yang, F. A.; Tung, C. Y. *Nanostruct. Mater.* **1995**, *6*, 977.

(14) Greiner, J. H.; Croll, I. M.; Sulich, M. *J. Appl. Phys.* **1961**, *32*, 188.

(15) Nogués, J.; Sort, J.; Langlais, V.; Doppiu, S.; Dieny, B.; Munoz, J. S.; Surinach, S.; Baro, M. D.; Stoyanov, S.; Zhang, Y. *Int. J. Nanotechnol.* **2005**, *2*, 23.

(16) Zheng, R. K.; Liu, H.; Wang, Y.; Zhang, X. X. *Appl. Phys. Lett.* **2004**, *84*, 702.

(17) Masala, O.; Seshadri, R. *J. Am. Chem. Soc.* **2005**, *127*, 9354.

(18) Fiévet, F. *Fine Particles: Synthesis, Characterization, and Mechanism Growth*; Sugimoto, T., Ed.; Marcel Dekker Inc.: New York, 2000.

(19) Ammar, S.; Helfen, A.; Jouini, N.; Fiévet, F.; Villain, F.; Rosenman, I.; Danot, M.; Molinié, P. *J. Mater. Chem.* **2001**, *10*, 186.

(20) Chkaoundali, S.; Ammar, S.; Jouini, N.; Fiévet, F.; Richard, M.; Villain, F.; Grenèche, J.-M.; Danot, M.; Molinié, P. *J. Phys: Condens. Matter* **2004**, *16*, 4357.

(21) Ammar, S.; Jouini, N.; Fiévet, F.; Grenèche, J.-M.; Danot, M.; Molinié, P. *J. Phys.: Condens. Matter* **2006**, *18*, 9055.

(22) Feldmann, C.; Metzmacher, C. *J. Mater. Chem.* **2001**, *11*, 2603.

(23) Poul, L.; Jouini, N.; Fiévet, F. *Chem. Mater.* **2000**, *12*, 3123.

(24) Taibi, M.; Ammar, S.; Jouini, N.; Fiévet, F. *J. Phys. Chem. Solids* **2006**, *67*, 932.

(25) Sicard, L.; Viau, G.; Ammar, S.; Herbst, F.; Mangeney, C.; Fiévet, F. *J. Mater. Chem.* **2008**, submitted.

(26) Poul, L.; Ammar, S.; Jouini, N.; Fiévet, F.; Villain, F. *J. Sol−Gel Sci. Technol.* **2003**, *26*, 261.

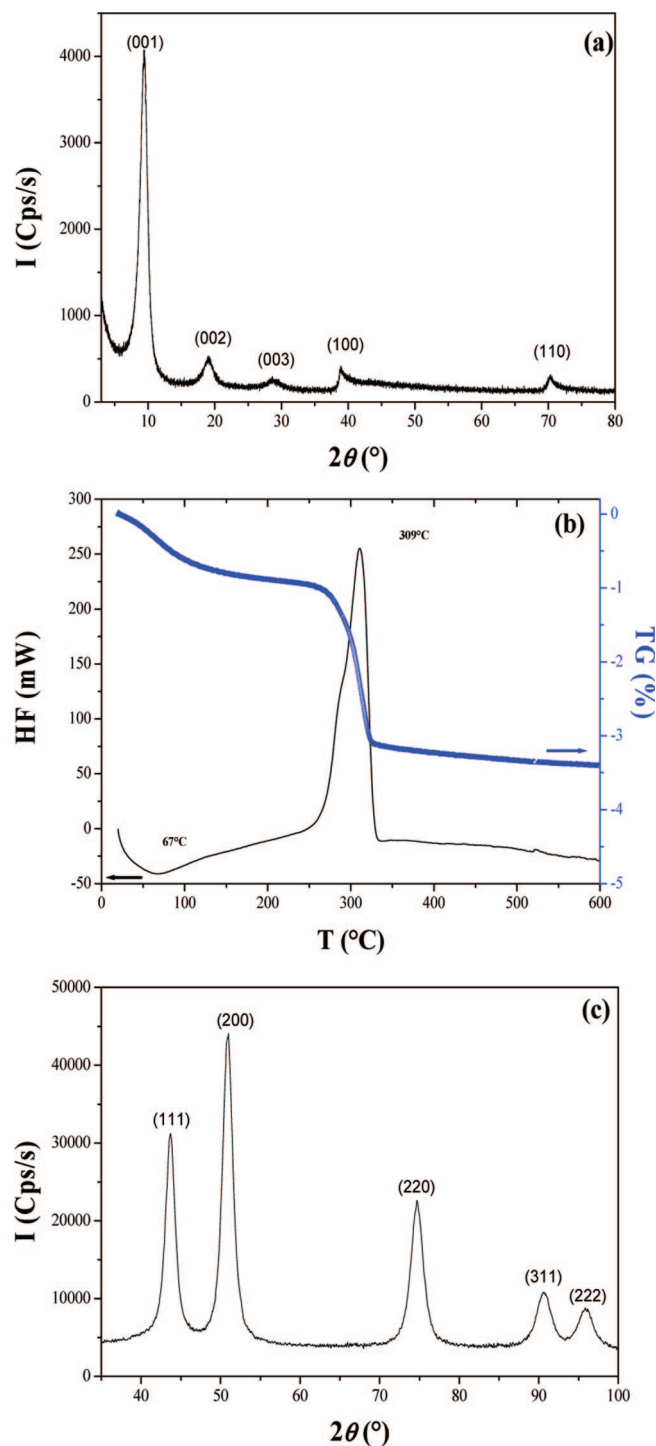(27) Taibi, M.; Ammar, S.; Jouini, N.; Fiévet, F.; Molinié, P.; Drillon, M. *J. Mater. Chem.* **2002**, *12*, 3238.

CoFe₂O₄ Nanoparticles Embedded in NiO Matrix

Chem. Mater., Vol. 20, No. 15, 2008 4863

Figure 1. XRD pattern (a) and DTA-TGA curves (b) of the as-made LHS sample and XRD pattern of its calcined product (c).

As previously announced in Introduction, 10 mg of the fresh $CoFe_2O_4$ particles was mechanically dispersed in 290 mg of alumina to prepare a reference sample of $CoFe_2O_4$ in a diamagnetic matrix with a weight fraction (3.33 wt %) close to the expected one for the NiO matrix.

Characterization. The crystalline structure of the powders was studied by X-ray diffraction (XRD) on a Panalytical X'pert Pro diffractometer equipped with a multichannel X'celerator detector, using Co Kα radiation ($\lambda = 1.7889$ Å) in the 2θ range of $5-100°$. The cell parameters of the produced phases were determined by Rietveld refinements,[28] and the crystallite mean size $\langle L \rangle$ was deduced from the XRD line broadening β (polycrystalline silicon

was used as a standard) by the Scherrer formula[29]

$$\langle L \rangle = \frac{0.9\lambda}{\beta \cos \theta} \quad (1)$$

The chemical composition of all the samples was checked by inductively coupled plasma-atomic emission spectroscopy (ICP) analysis performed at the CNRS Analysis Center in Vernaison.

The size and shape of the particles were analyzed on a JEOL-100-CX II transmission electron microscope operating at 100 kV. The particle size distribution was obtained from the transmission electron microscopy (TEM) images using a digital camera and the SAISAM software (Microvision Instruments), calculating the surface-average particle diameter d_p from eq 2

$$d_p = \sum_i n_i d_i^2 / \sum_i n_i d_i \quad (2)$$

where n_i is the number of particles with d_i diameter. The statistical result of the particle size was obtained by counting ca. four hundred particles considering a spherical particle shape. d_p is given in nanometers. High-resolution microscopy also was performed using a JEOL-2010 UHR microscope operating at 200 kV.

Energy filtered imaging (EFI) was performed on a transmission electron microscope JEOL 2100 FEG UHR with a Gatan Imaging filter 2001. The three window technique was used for elemental mapping: two images were taken below the edge and one on the edge. The edge background was determined by a power law method using the two pre-edge images and subtracting the edge image to obtain the true edge signal. The map intensity is proportional to the projected concentration of the element.

Thermogravimetric and differential thermal analyses (TGA and DTA) were carried out with a heating rate of 5 °C min^{-1} in an alumina crucible under air with a Setaram TG92-12 thermal analyzer. Nitrogen adsorption and desorption isotherms were obtained at 77 K using a Micromeritics ASAP 2010 apparatus. The samples were outgassed at 373 K and 0.1 MPa for 12 h before measurements. Specific surface area (S_{BET}) values were obtained using the Brunauer–Emmett–Teller equation.[30]

A Quantum Design MPMS-5S super quanducting interference device (SQUID) magnetometer was used for magnetic characterization in the 5–310 K temperature range. The thermal zero-field cooling (ZFC) and field cooling (FC) dc susceptibility, χ, variations were measured in a magnetic field of 200 Oe. ZFC isothermal magnetization also was measured at 5 K by cycling the magnetic field, **H**, between +50 and −50 kOe. To highlight the existence of an exchange bias in some samples, a measurement of the isothermal magnetization at 5 K, after cooling from room temperature, under a field of 50 kOe, also was performed. The same magnetometer was employed to take ac χ data (5–300 K) at various frequencies ($\nu = 1$ and 1000 Hz) in a field strength of 1 Oe.

Results and Discussion

Characterization of Nickel LHS before and after Thermal Treatment. The synthesized material presents a typical X-ray diffraction pattern (see Figure 1a) of a layered hydroxyacetate nickel salt as previously described by Poul et al.[23] and Taibi et al.[27] It consists of a brucite-like structure with a turbostratic disorder. The XRD pattern exhibits symmetrical reflections (00*l*) at low angles and two (*hk*0)

(28) Rodriguez-Carvajal, J. *FULLPROF*; Laboratoire Léon Brillouin CEA-CNRS: Grenoble, 1998.
(29) Warren, E. *X-ray Diffraction*; Addison-Wesley: New York, 1969.
(30) Brunauer, S.; Emmett, P. H.; Teller, E. *J. Am. Chem. Soc.* **1938**, *60*, 309.

Table 1. Chemical Composition of All Produced Samples Inferred from ICP Analysis

sample	Ni (wt %)	Co (wt %)	C (wt %)	Co/Ni atomic ratio	CoFe$_2$O$_4$ (wt %)
LHS	45.20		10.34		
CoFe$_2$O$_4$		19.30	1.50		
LHS/CoFe$_2$O$_4$	42.20	0.48	12.60	0.011	1.88
NiO/CoFe$_2$O$_4$	69.55	0.94		0.013	3.75

Table 2. Main Magnetic Characteristics of All Produced Samples

sample	M_{50kOe} (5 K) (emu g^{-1})[a]	H_c (5 K) (kOe)[b]
LHS	86.5	0.74
LHS/CoFe$_2$O$_4$	81.5	0.76
CoFe$_2$O$_4$ in Al$_2$O$_3$	2.1	8.85
NiO/CoFe$_2$O$_4$	2.0	7.40

[a] Expressed per gram of powder. [b] Measured on the ZFC magnetization hysteresis.

asymmetrical reflections at high angles. The asymmetry of the in-plane reflections is due to the turbostratic character: the stacking order of brucite-like sheets is parallel and equidistant along the *c* axis of the hexagonal cell but twisted against each other. This turbostratic character is often observed for layered hydroxide-based materials prepared by chimie douce routes.[23,31] The parameter *c* corresponding to the interlayer spacing is deduced from the peak position of the (001) reflection. It is found to be 10.90 Å, which is in good agreement with the previously reported value.[23,27] The parameter *a*, corresponding to the Ni−Ni distance within the layer, is equal to 3.09 Å. It was calculated using the (100) reflection peak position, and it also was found to be close to the previously reported value.[23,27]

Chemical analysis, given in Table 1, permits us to confirm the composition of LHS, Ni(OH)$_{1.6}$(CH$_3$CO$_2$)$_{0.4}$·n(H$_2$O), which is close to that previously reported.[23,27]

The TGA curve of the LHS phase is given in Figure 1b. It presents several weight losses. The first weight loss is endothermic. It occurs in the temperature range of 40−150 °C. It is due to the departure of adsorbed and intercalated water. The second weight loss is exothermic. It occurrs in the temperature range of 150−325 °C. It is mainly assigned to the dehydroxylation of the brucite-like sheets, leading to the formation of NiO, as confirmed by XRD. The calcination of the intercalated acetate ions occurs also in the same temperature range. On the basis of these results, the temperature of calcination of the LHS phase was fixed at 300 °C (573 K). The thermal treatment was carried out under air flow, the heating being maintained for 24 h to reach the total transformation of the LHS phase into NiO on the one hand and to favor better structural contact between the CoFe$_2$O$_4$ core and the NiO shell on the other hand. With such a long heating time, the two phases should be in close contact and the interface should present a low defect concentration and low strain. The XRD pattern of the calcined sample (Figure 1c) corresponds undoubtedly to the cubic face centered NiO phase with no preferred orientation and no discernible impurities. The cell parameter inferred from Rietveld refinements (*a* = 2.952 Å) agrees well with that of JCPDS file no. 01-071-1179. The large width of the XRD peaks

suggests that the crystallites are very small. Applying the Scherrer formula for isotropic particles, the inferred average crystal size was found to be ∼10.6 nm.

Electron microscopy revealed significant morphological differences between the as-synthesized LHS phase and its calcined product. On the one side, the LHS compound exhibited typical characteristics of a turbostratic layered material: it appears as an aggregate of thin crumpled sheets without any definite shape (Figure 2a). On the other side, the final oxide phase appears as aggregates of monodisperse and almost isotropic nanoparticles with an average diameter of 8.3 ± 2.0 nm (Figure 2b). The particles can be considered as single crystals since their diameter agrees fairly well with the average crystallite size. High-resolution microscopy showed that the particles are well-crystallized (see Figure 3). There is no evidence of stacking faults or dislocations, and the fringes correspond to crystallographic planes of the cubic lattice of the nickel oxide structure. Indeed, the diffraction pattern calculated from the high-resolution image corresponds to the <101> zone axis (Figure 3) with a cell parameter in agreement with the one determined by XRD analysis.

Characterization of CoFe$_2$O$_4$ Nanoparticles before and after Thermal Treatment. For a better comprehension of the magnetic properties of the desired CoFe$_2$O$_4$/NiO composite material, the starting cobalt ferrite nanoparticles used for the preparation of the sol and their thermally treated counterpart were characterized by ICP (Table 1), XRD (Figure 4), and TEM (Figure 5). The treatment was of course carried out under the same conditions as those of LHS and LHS/CoFe$_2$O$_4$. As expected, the powder recovered by centrifugation corresponds to the CoFe$_2$O$_4$ phase, which crystallizes in a cubic spinel structure with a cell parameter (*a* = 8.390 Å) close to that of bulk ferrite (*a* = 8.395 Å).[32] There is no significant variation in the *a* value after calcination (*a* = 8.392 Å). A large peak width, due to the small size of the particles, is observed for both samples. However, it is less pronounced in the calcined powder, indicating that the crystal size increases during calcination. The average crystal size, calculated for each sample by the Scherrer formula, was found for the raw nanoparticles and the calcined particles to be ∼3.9 and 7.2 nm, respectively. These values are slightly larger than those deduced from TEM observations, which shows particles uniform in shape and size with an average diameter of ∼2.5 ± 0.3 and 5.0 ± 1.5 nm, respectively. These differences are mainly due to the fact that the determination of the particle size by XRD is based on a volume calculation, while it is based on a surface one by TEM (Figure 5). The as-made particles appear in the micrographs as being less agglomerated than the calcined particles. High-resolution microscopy (Figure 6) showed that the particles are highly crystalline single crystals.

LHS Synthesized in Presence of Nanoparticles. Owing to the aim of this work, it is essential to verify that

(31) Tekaia Ehlsissen, K.; Delahaye-Vidal, A.; Genin, P.; Figlarz, M.; Willmann, P. *J. Mater. Chem.* **1993**, *3*, 883.
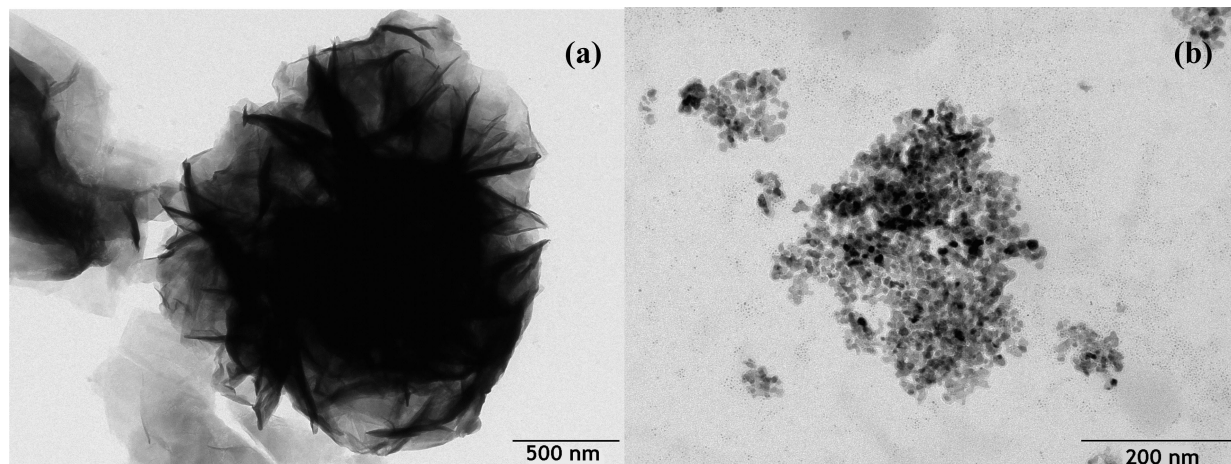(32) Valenzuela, R. *Magnetic Ceramics*; Cambridge University Press: New York, 1984..

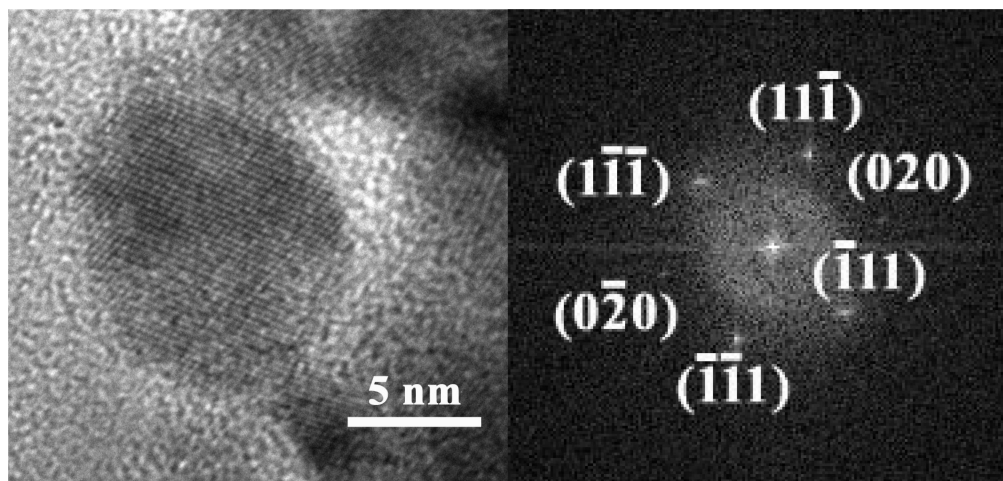**Figure 2.** TEM micrographs of the LHS (a) and NiO (b) samples.

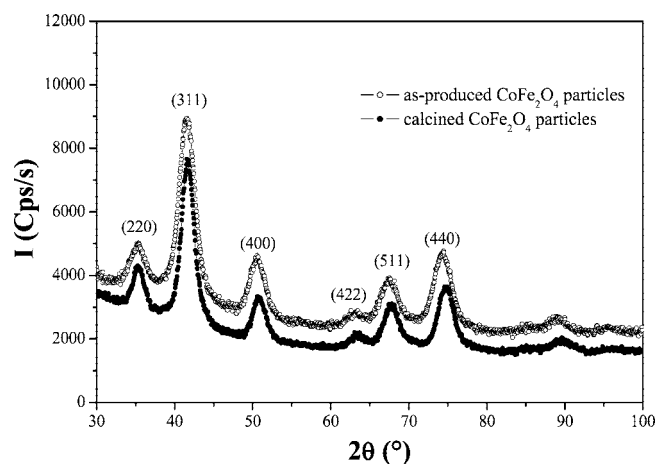**Figure 3.** HRTEM image of a single crystal of NiO and its FFT pattern (<101> zone axis).

Figure 4. XRD patterns of as-produced and calcined CoFe$_2$O$_4$ particles.

CoFe$_2$O$_4$ nanoparticles are present in the intermediate composite, and for a better control of the microstructure of the final product, it is important to determine if they are intercalated between the layers of the LHS or just adsorbed on the external surface of the material. Contrary to pure LHS, which is a green powder, the dried product obtained after precipitation of LHS in the presence of CoFe$_2$O$_4$ particles is brown. The XRD pattern of the

resulting composite (Figure 7a) presents only peaks due to the LHS phase. There is no displacement of the 2θ positions of the diffraction peaks to lower values, which could be an indication of a larger interlamellar distance and then an effective periodic intercalation of the CoFe$_2$O$_4$ particles. The peaks are just broadened due to poor crystallinity and small crystallite sizes. The absence of the peaks related to the CoFe$_2$O$_4$ phase in the pattern can be explained by the low amount of nanoparticles in the final product (lower than the XRD detection limit). ICP analysis agrees with this conclusion. Indeed, the Co/Ni atomic ratio is found to be 0.011 in the LHS/CoFe$_2$O$_4$ composite (see Table 1). After calcination, the XRD pattern is similar to that of the calcined LHS (Figure 7b). It corresponds to a NiO phase constituted by small crystallites of ∼10 nm as suggested by the peak width. The ferrite phase is still not visible; nevertheless, its presence is confirmed by ICP analysis. The weight fraction of CoFe$_2$O$_4$ in the final composite is ∼3.74%.

The TEM micrograph of the as-produced LHS/CoFe$_2$O$_4$ composite (Figure 8a) is different from that of pure LHS. The LHS sheets are no longer aggregated. They now stand alone. Some ferrite particles are present adsorbed on or intercalated in the layer of LHS. The calcined sample is constituted of almost spherical 10 nm sized particles (9.6
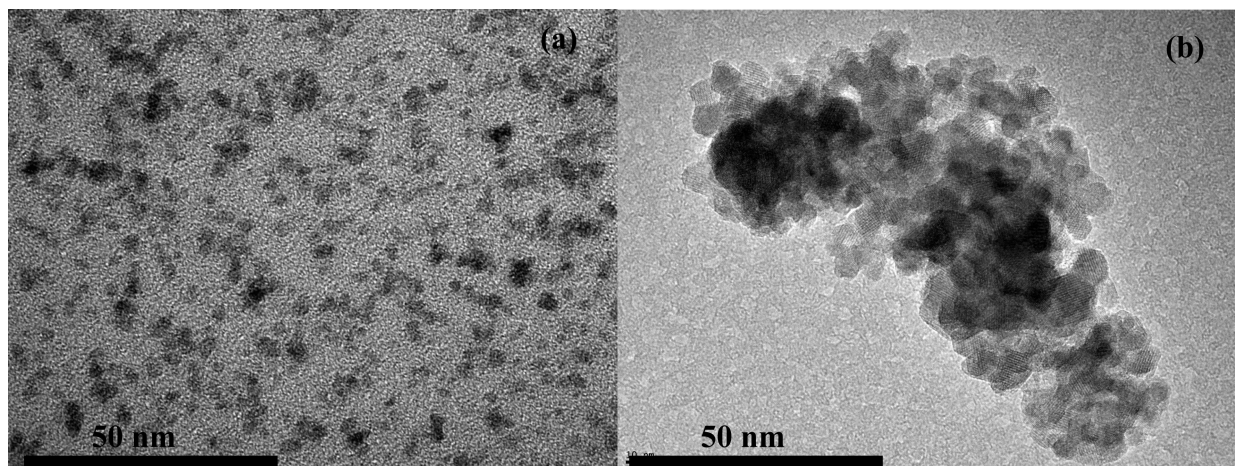
Figure 5. TEM micrographs of as-produced (a) and calcined (b) CoFe$_2$O$_4$ particles.
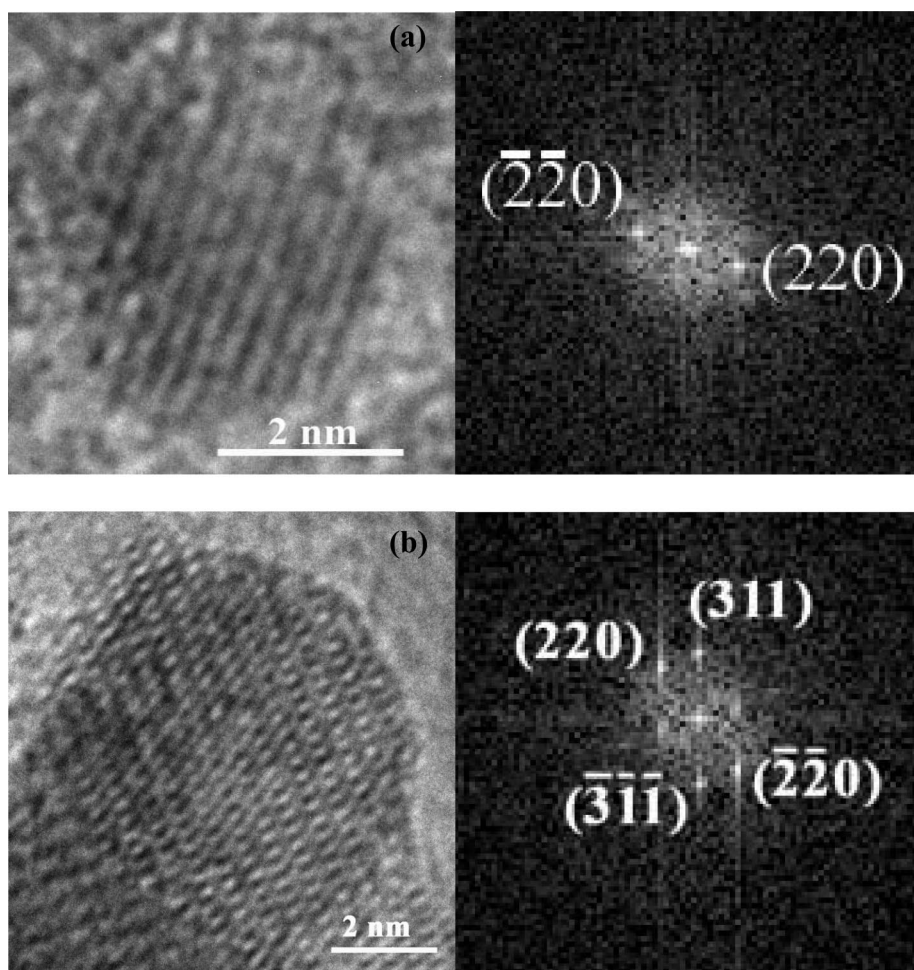

Figure 6. HRTEM images of some representative CoFe$_2$O$_4$ particles before (a) and after (b) calcination. FFT patterns of the selected areas are given as well.

± 2.3 nm). All the observed particles have almost the same diameter. The agglomeration of the 2.5 nm CoFe$_2$O$_4$ particles to form ∼5 nm ones, as previously observed in Figure 6, is absent. There are no free cobalt ferrite particles with diameters of 2.5 nm on the different observed grids. However, it is not clear from the images if the calcined composite forms a core−shell structure. Because of their structural proximity, high-resolution images do not distinguish between the NiO and the CoFe$_2$O$_4$ phases. Both

are cubic face centered, and several of their reticular distances are close to each together. We performed TEM and EFI coupled imaging. Figure 9 shows a TEM micrograph of a quite representative area of the sample, as well as its Ni, Co, and O mapping. These images show that, despite a very weak contrast on cobalt because of its too low concentration, Co and Ni are localized almost uniformly all over the material just like oxygen, indicating that NiO and CoFe$_2$O$_4$ do not necessarily form a core−shell
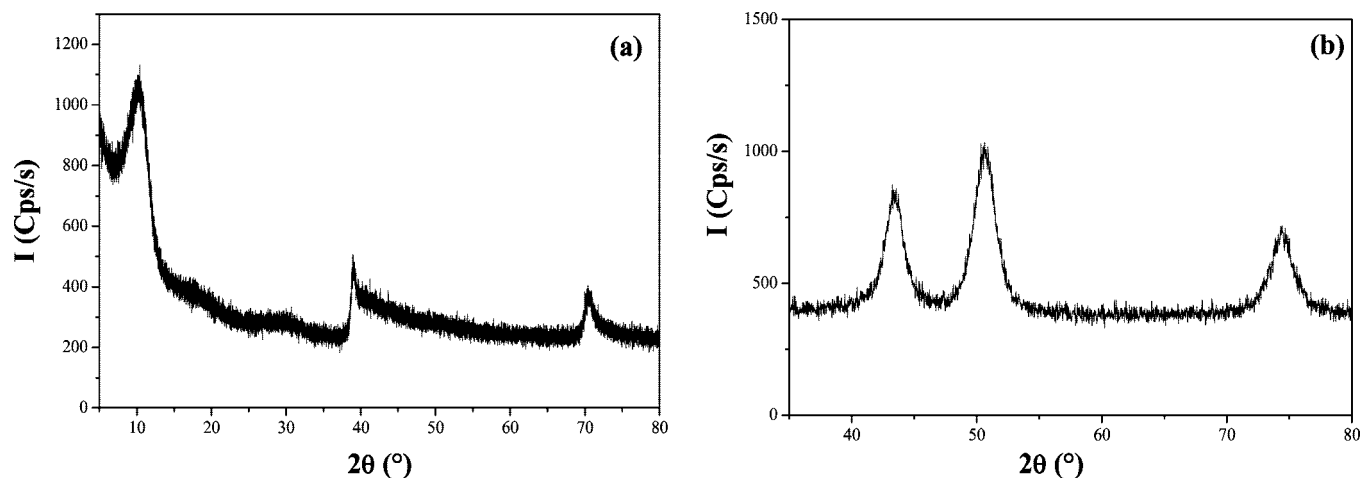
Figure 7. XRD patterns of LHS/CoFe₂O₄ (a) and NiO/CoFe₂O₄ composites (b).
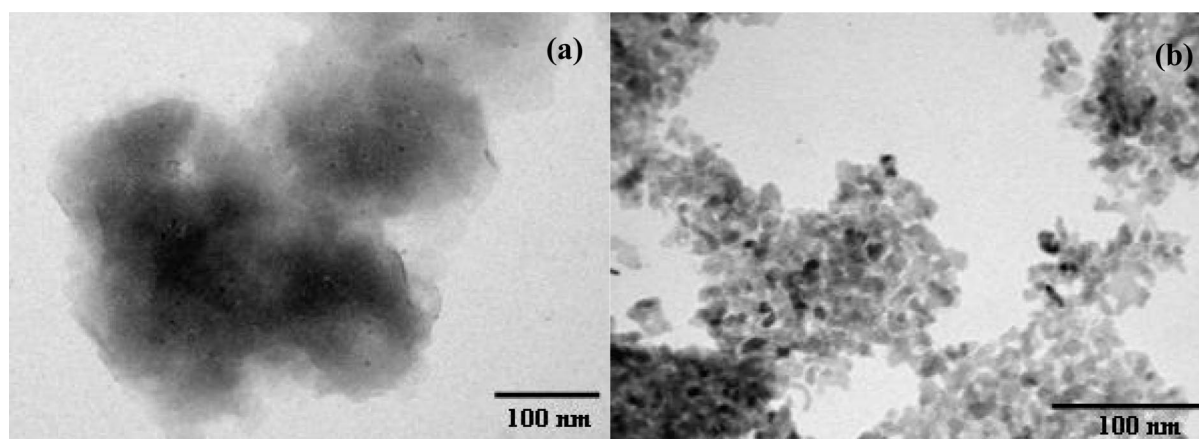

Figure 8. TEM micrographs of LHS/CoFe₂O₄ (a) and NiO/CoFe₂O₄ (b) composites.

structure, but certainly a nanostructure where CoFe₂O₄ nanocrystallites are embedded in a NiO matrix. Moreover, the particle size distribution of the obtained particles (Figure 10a) is greater than that of NiO ones produced by direct calcination of LHS (Figure 10b), namely, 9.6 ± 2.3 nm inside of 8.5 ± 2.0 nm. Such a feature already was observed in Mn−Mn₃O₄ nanocomposites exhibiting an exchange bias[46] with a nanostructure very probably close to a core−shell arrangement. On the basis of all these observations, we conclude to favor the same kind of nanostructure.

N₂ adsorption−desorption isotherms of as-produced LHS and LHS/CoFe₂O₄ composite are presented in Figure 11a. Although a hysteresis loop was observed for the two materials, the isotherms cannot be classified as type IV isotherms because no plateau can be detected at high relative pressures, which is an indication of mesopores filling. As recommended by Rouquerol et al.,[33] they are rather termed type IIb isotherms, which are observed with plate-like particles. LHS and the LHS/CoFe₂O₄ composite exhibit similar specific surface area values: 31 and 34 m² g⁻¹, respectively. The relatively low C constant values, respectively, 47 and 73, suggest that the materials contain no microporosity. However, the two isotherms differ markedly above P/P^0 of ∼0.5, indicating important textural changes after incorporation of the CoFe₂O₄ nanoparticles. Indeed, for

the LHS solid, a wide hysteresis loop of type H2 with a steep decrease at P/P^0 near 0.5 for the desorption branch clearly is observed, whereas for the composite, the hysteresis is rather of type H3 according to the IUPAC classification.[34] Moreover, the pore size distributions (see Figure 11b) obtained with the desorption branch data, using the Barrett−Joyner−Halenda (BJH) method,[35] reveal that an average pore diameter of ∼3.4 nm can be found for the two materials, even if the dV/dD pore volume is ∼10 times less for LHS/CoFe₂O₄ than for the LHS solid. This value is not related to the interlayer spacing since the (001) distance was found to be 10.90 Å by XRD. The TEM results clearly show that the sand-rose structure was lost after incorporation of the particles even if the LHS phase was still present as evidenced by XRD. These results are tentatively explained considering that for the LHS material, the large hysteresis loop results from porosity existing between the aggregates of plate-like particles. After incorporation of CoFe₂O₄ particles, the sand-rose structure was lost, leading to a

(33) Rouquerol, F.; Rouquerol, J.; Sing, K. *Adsorption by Powders and Porous Solids: Principles, Methodology, and Applications*; Academic Press: San Diego, 1999; p 365.
(34) Sing, K. S. W.; Everett, D. H.; Haul, R. A.; Moscou, L.; Pierotti, R. A.; Rouquerol, J.; Siemieniewska, T. *Pure Appl. Chem.* **1985**, *57*, 603.
(35) Barret, E. P.; Joyner, L. G.; Halenda, P. P. *J. Am. Chem. Soc.* **1951**, *73*, 376.
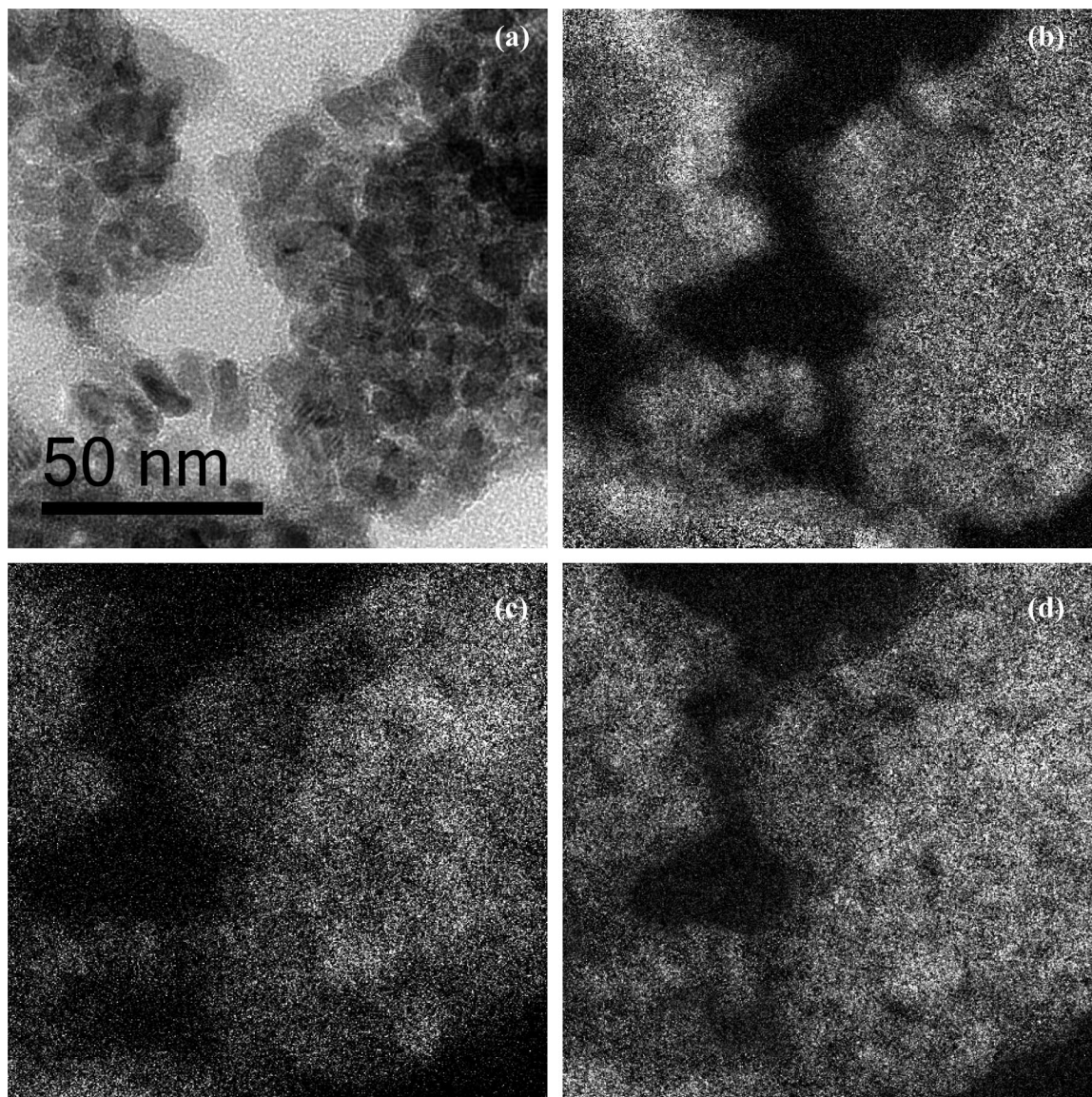
Figure 9. TEM micrograph of NiO/CoFe$_2$O$_4$ composite (a) with its EFI Ni (b), Co (c), and O (d) mapping.

significant decrease of textural porosity. These particles are adsorbed at the surface of the LHS crystallites.

Magnetic Properties. The thermal variation of the dc susceptibility of as-produced LHS and LHS/CoFe$_2$O$_4$ and that of CoFe$_2$O$_4$ dispersed in alumina and NiO/CoFe$_2$O$_4$ are given in Figure 12a,c, respectively. All data are plotted per gram of powder. The in-phase (χ') and out-of-phase (χ'') components of the ac susceptibility measured at different frequencies (1 and 1000 Hz) on the LHS/CoFe$_2$O$_4$ and the NiO/CoFe$_2$O$_4$ composites also are given in Figure 12b,d, respectively.

As expected, the LHS phase exhibited ferromagnetic behavior characterized by a rapid increase of FC-dc-$\chi(T)$ at low temperatures to reach a kind of plateau when the temperature decreased below the Curie temperature T_C, while ZFC-dc-$\chi(T)$ exhibits a slight maximum (Figure 12a).[27] The appearance of a maximum in the ZFC curve is due to a kind of magnetic viscosity that is usually observed in such a layered hydroxide. The T_C value deduced from the maximum of the in-phase (χ') and out-of-phase (χ'') components of the ac susceptibility measured at different frequencies was
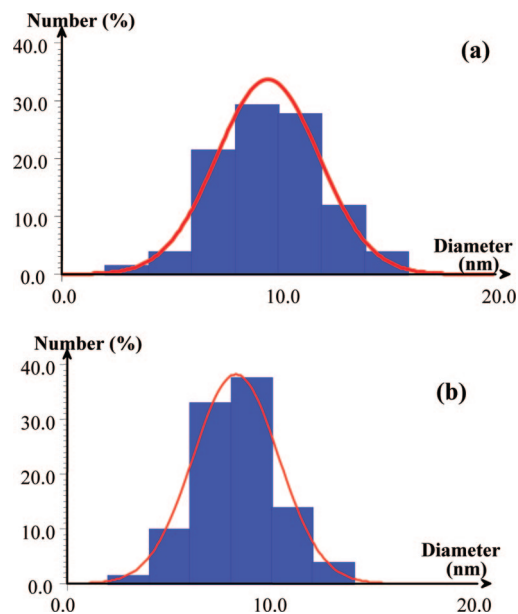

Figure 10. Particle size distribution of NiO/CoFe$_2$O$_4$ (a) and NiO (b).

CoFe₂O₄ Nanoparticles Embedded in NiO Matrix

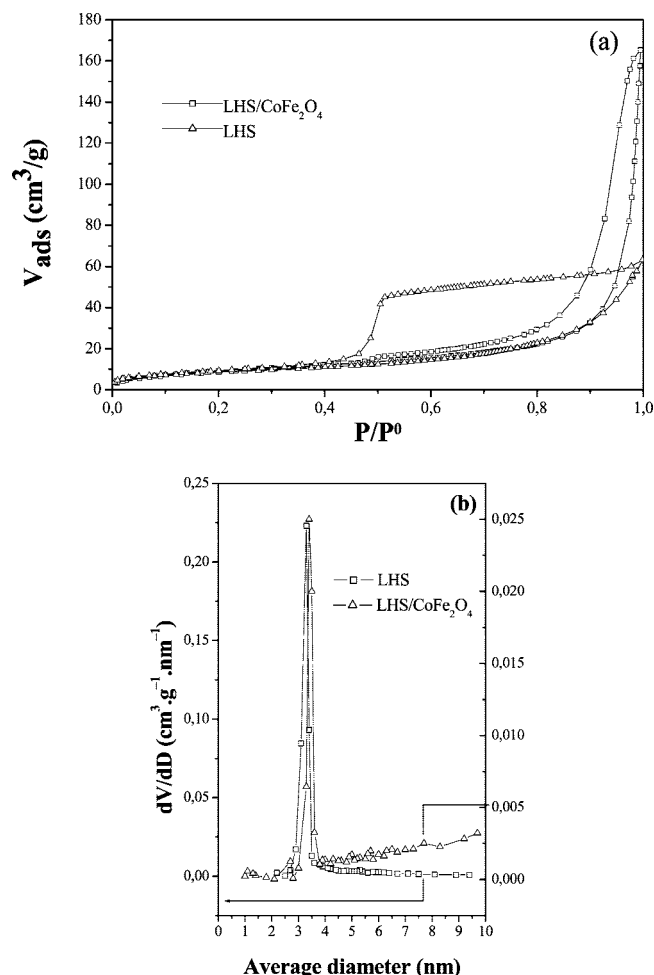*Chem. Mater., Vol. 20, No. 15, 2008* 4869

Figure 11. N_2 adsorption and desorption isotherms (a) and BJH pore size distributions (b) of LHS and LHS/CoFe₂O₄ samples.

found to be equal to 16 K (not shown) in agreement with previous works devoted to hydroxyacetate nickel salt prepared in polyol.[27] The LHS/CoFe₂O₄ composite exhibited the same behavior with the same T_C value (Figure 12a). The T_C value was determined from the maximum of the $\chi'(T)$ and $\chi''(T)$ curves measured at different frequencies from 1 to 1000 Hz (Figure 12b). These results suggest that the ferrite nanoparticles do not affect the magnetic interaction between the layers in the lamellar compound. This is supplementary proof of the location of these particles at the surface of the LHS crystallites rather than their intercalation in the interslabs. An enlargement of the ZFC-dc-$\chi(T)$ curve of the LHS/CoFe₂O₄ composite (see the inset of Figure 12a) exhibits another maximum at higher temperatures, around 125 K, attributed by comparison to that of Figure 12c, to the magnetic contribution of CoFe₂O₄ nanoparticles. Indeed, these particles are superparamagnets. When they are dispersed in alumina, their ZFC-dc-$\chi(T)$ curve shows a cusp at a critical temperature corresponding to the blocking temperature, T_B, which is here equal to 130 K and decreases rapidly to zero at lower temperatures, while FC-dc-$\chi(T)$ increases slightly as the temperature decreases. The good superposition of these curves with those of the composite around this temperature confirms the presence of particles in the labeled LHS/CoFe₂O₄ sample. The FC-dc-$\chi(T)$ contribution of the CoFe₂O₄ particles in the LHS/CoFe₂O₄

composite at low temperatures cannot be distinguished from that of LHS owing to the strong magnetization of the latter. This is quite disappointing because usually the shape of the FC-dc-$\chi(T)$ curve below T_B is used to appreciate the occurrence of dipolar interactions between superparamagnets (here the CoFe₂O₄ particles). Indeed, in concentrated superparamagnetic samples, FC magnetization is flattened below T_B due to strong interparticle interactions, while in diluted ones, the FC curve shows an increase below T_B.[36–38] Some authors claimed that the FC-dc susceptibility must continue to rise monotonously with a temperature decrease below T_B for noninteracting superparamagnets, and a deviation from such variation evidences interparticle interactions.[39,40]

Nevertheless, an enlargement of the thermal variation of the χ' and χ'' components of the ac susceptibility measured at different frequencies ($\nu = 1$ and 1000 Hz) exhibited a second maximum related to the presence of the nanoparticles, which is frequency dependent. The temperature of the maximum (T_{max}) for each component increases with increasing frequency. Such behavior is usually observed in superparamagnets.[41] The frequency shift per units of 10 of the maximum out-of-phase ac susceptibility versus T was used to calculate a quantity ϕ defined according eq 3, which usually permits the appreciation of the strength of the interparticle magnetic interactions[42]

$$\varphi = (\Delta T_{max}/(T_{max} \Delta\log(2\pi\nu))) \qquad (3)$$

where ϕ is of the order of 8×10^{-2}, which is close to 10^{-1}, the typical value for noninteracting superparamgnets, suggesting that the CoFe₂O₄ particles are still interacting but that the interparticle interactions (mainly dipolar) can be considered as weak.[42] Obviously, the fixed CoFe₂O₄ weight fraction in the composite is low enough to reduce this kind of interaction.

This is not the case for the CoFe₂O₄ particles mechanically dispersed in diamagnetic Al₂O₃ (Figure 12c). The FC-dc susceptibility in this reference sample increases below T_B and tends to reach a plateau at low temperatures, traducing the fact that the particles are more strongly interacting, despite a very weak CoFe₂O₄ weight fraction. One can suppose that the mechanical procedure used to disperse the superparamagnets in the diamagnetic matrix is not so efficient and does not allow a real separation between all the mixed nanoparticles in alumina. Unfortunately, ac susceptibility measurements performed on this sample did not permit us to calculate ϕ, due to a very weak signal-to-noise ratio in relation to the large diamagnetic weight fraction of alumina in the sample. Besides these experimental results, all the specialists agree that the dipolar interactions play a very important role in the magnetic behavior of superparamagnets and still affect their properties when they are not sufficiently diluted, the limit dilution ratio not being precisely defined. For instance, it was recently evidenced that Co nanoparticles embedded in a diamagnetic Ag matrix prepared in the form of a thin film by coprecipitation using a gas aggregation cluster source and a molecular beam epitaxy source were still interacting despite a very low weight fraction.[43]

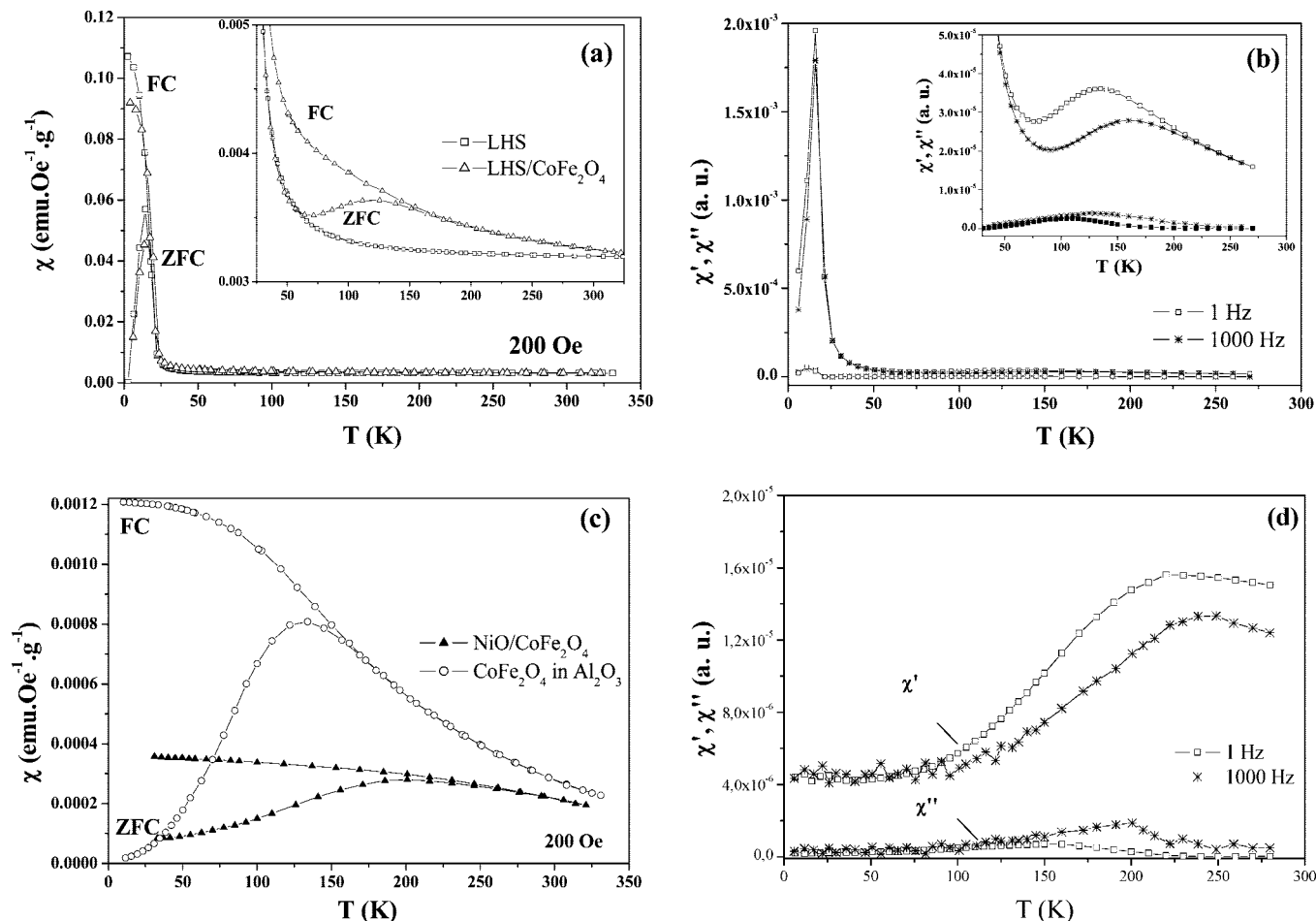(36) Bajpai, A.; Banerjee, A. *Phys. Rev. B: Condens. Matter Mater. Phys.* **2000**, *62*, 8996.

Figure 12. Thermal variation of ZFC and FC dc susceptibility of LHS and LHS/CoFe$_2$O$_4$ (a). Thermal variation of ZFC in-phase and out-of-phase ac suscpetibility of LHS/CoFe$_2$O$_4$ at different frequencies (b). Thermal variation of ZFC and FC dc susceptibility of CoFe$_2$O$_4$ in Al$_2$O$_3$ and NiO/CoFe$_2$O$_4$ (c). Thermal variation of ZFC in-phase and out-of-phase ac suscpetibility of NiO/CoFe$_2$O$_4$ at different frequencies (d). An enlargement of the high-temperature region is given in the inset of panels a and b.

The comparison of the thermal variation of the dc susceptibility of CoFe$_2$O$_4$ particles embedded in NiO to that of the same particles dispersed in Al$_2$O$_3$ reveals notable differences. The superparamagnetic behavior of the particles is still maintained, as evidenced by a net irreversibility between the FC- and the ZFC-dc-$\chi(T)$ curves (Figure 12b), but the blocking temperature, measured at the maximum of the ZFC-dc-$\chi(T)$ curve, is significantly shifted to higher temperatures. T_B of the 2.5 nm CoFe$_2$O$_4$ particles embedded in the NiO antiferromagnet is ∼200 K, while it does not exceed 130 K for the same particles mechanically dispersed in the Al$_2$O$_3$ diamagnet. This T_B enhancement can be attributed to exchange bias contribution. Moreover, the FC-dc susceptibility increases slowly,

when T decreases below T_B, and it does not go to saturation at very low temperatures. Such a variation should be an indication that the interparticle interactions are still present but that they are very probably weaker than those in CoFe$_2$O$_4$ dispersed in the alumina sample. The thermal variation of the ac susceptibility of this sample is given in Figure 12d. It shows a clear frequency dependence of the maximum of the χ' and χ'' components. The quantity ϕ defined by eq 3 here is equal to 8×10^{-2}, suggesting as previously observed for the LHS/CoFe$_2$O$_4$ composite that the CoFe$_2$O$_4$ superparamagnets are still slightly interacting in the NiO/CoFe$_2$O$_4$ composite.

Another difference between the two samples comes from the magnetic dc susceptibility value. It is, at a given temperature, for the CoFe$_2$O$_4$ particles in Al$_2$O$_3$ (weight fraction of 3.33%) always higher than that for CoFe$_2$O$_4$ particles embedded in NiO (weight fraction of 3.75%). This may be due to the antiferromagnetic character of NiO, in which susceptibility is a decreasing function of the temperature at $T < T_N$ ($T_N = 525$ K).[44]

The ferromagnetic character of LHS and LHS/CoFe$_2$O$_4$ as well as the ferrimagnetic character of CoFe$_2$O$_4$ in alumina samples are evidenced by the presence of a hysteresis loop in the variation of ZFC magnetization, expressed per gram of powder, when cycling the magnetic field at 5 K (Figure

(37) Denardin, J. C.; Brandl, A. L.; Knobel, M.; Panissod, P.; Pakhomov, A. B.; Liu, H.; Zhang, X. X. *Phys. Rev. B: Condens. Matter Mater. Phys.* **2002**, *65*, 64422.
(38) Makhlouf, S. A.; Parker, F. T.; Berkowitz, A. E. *Phys. Rev. B: Condens. Matter Mater. Phys.* **1997**, *55*, 14717.
(39) Walmsley, R. N.; Chantrell, W.; Gore, J.; Maylin, M. *J. Phys. D: Appl. Phys.* **2000**, *33*, 784.
(40) Mørup, S.; Hansen, M. F. *Handbook of Magnetism and Advanced Magnetic Materials*; John Wiley and Sons: New York, 2007.
(41) Fiorani, D.; Testa, A. M.; Tronc, E.; Lucari, F.; D'Orazio, D.; Nogués, M. *J. Magn. Magn. Mater.* **2001**, *226–230*, 1942.
(42) Dormann, J. L.; Bessais, L.; Fiorani, D. *J. Phys. C* **1988**, *21*, 2015.
(43) Domingo, N.; Testa, A. M.; Fiorani, D.; Binns, C.; Baker, S.; Tejada, J. *J. Magn. Magn. Mater.* **2007**, *316*, 155.
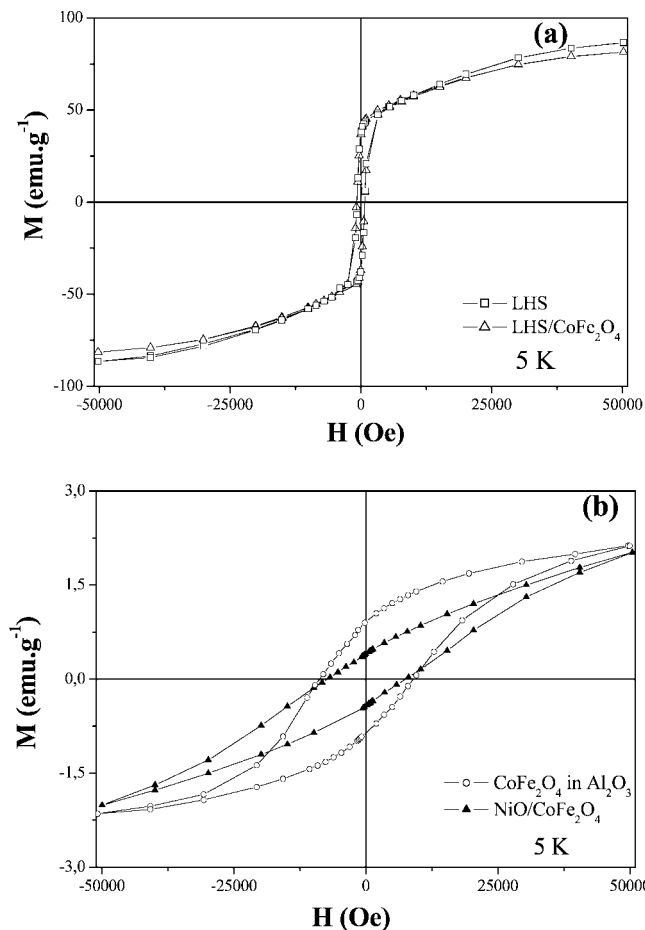
Figure 13. 5 K ZFC magnetization as a function of the magnetic field of LHS and LHS/CoFe₂O₄ (a) and CoFe₂O₄ in Al₂O₃ and NiO/CoFe₂O₄ (b) samples.

13). The magnetization of the LHS sample measured at a field as high as 50 kOe was ∼86.5 emu g^{-1}, corresponding to 1.7 μ_B per mol of Ni^{2+}. This value is very close to the 2 μ_B/Ni expected for an oxygen coordinated Ni^{2+} ion in brucite-like sheets. The obtained value for LHS/CoFe₂O₄, namely, 81.5 emu g^{-1}, is slightly lower. This reduction of the magnetization value is mainly due to two reasons: first, the lower magnetic contribution of CoFe₂O₄ particles (see Figure 13b) and second, the poor crystallinity of the layered phase in the composite (see Figure 7a).

The results of the 5 K ZFC magnetization for CoFe₂O₄ particles embedded in NiO in comparison to those of the CoFe₂O₄ particles dispersed Al₂O₃ are plotted in Figure 13b. They show a hysteresis symmetrical loop in both cases with an increase of the coercivity from the first to the second. H_c is ∼7.40 and 8.85 kOe, respectively. The magnetization does not saturate and continues to increase quasi-linearly with the field for the first, whereas it tends to do so for the second. Such differences can be explained within the following picture. On one hand, the large NiO content, which is an antiferromagnet below 525 K,[44] affects the **M(H)** shape curve at high field in the composite, and on the other hand, the interface exchange coupling between the CoFe₂O₄ particles and the antiferromagnetic NiO matrix producing exchange bias affects the **M(H)** shape curve at low field. Moreover, the presence of an exchange bias also implies a shift of the
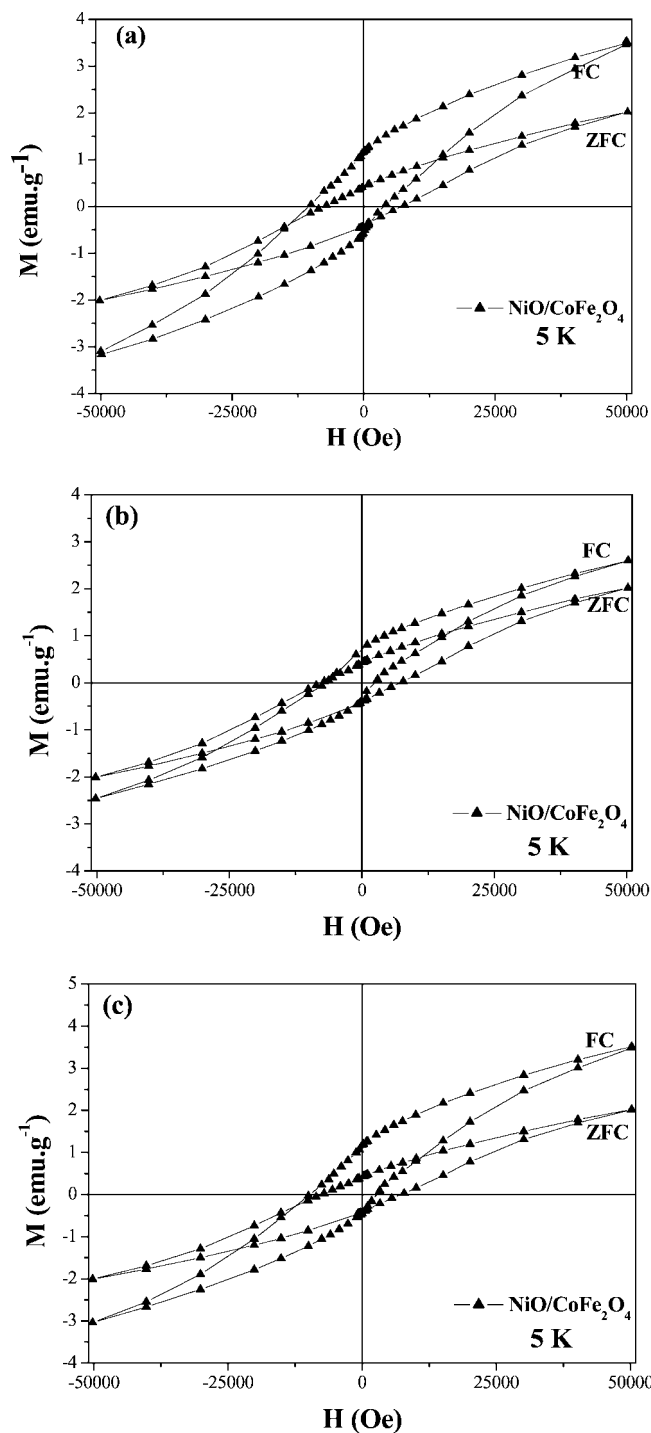

Figure 14. 5 K FC and ZFC magnetization as a function of magnetic field of the NiO/CoFe₂O₄ composite. Note that FC measurements were performed with an applied cooling of 50 kOe (a), 15 kOe (b), and 70 kOe (c).

loop in the field axis and a change of the coercivity when the sample is cooled under an applied field (FC) from room temperature (see Figure 14a). The values of the exchange field **H**$_{eb}$ and the coercivity, **H**$_c$(FC), are defined as[45]

$$H_c(FC) = (-H_{c-} + H_{c+})/2 \qquad (4)$$

$$H_{eb} = -(H_{c-} + H_{c+})/2 \qquad (5)$$

where **H**$_{c+}$ and **H**$_{c-}$ are the positive and negative values of the coercivity, respectively. **H**$_{eb}$ and **H**$_c$(FC) are found to be 3.28 and 7.20 kOe, respectively, corresponding to an **H**$_{eb}$/**H**$_c$ ratio of 0.46.

We observed also a dependence of the exchange bias field by varying the cooling field for the 5 K FC magnetization loop measurement. When the cooling field is fixed to 15 kOe, the vertical and horizontal FC hysteresis shifts decrease with an H_{eb} value of 2.17 kOe (Figure 14b). When the cooling field is fixed to 70 kOe, the vertical and horizontal FC hysteresis shifts increases with an H_{eb} value of 3.57 kOe (figure 14c). We note that H_{eb} increases when the cooling field increases and seems to reach a kind of saturation for the higher cooling field values. Such dependence on H_{eb} also was observed in various nanostructures, for instance, in antiferromagnetic MnO/ferrimagnetic Mn_3O_4 core/shell nanoparticles[46] and in ferromagnetic Fe nanoparticles embedded in antiferromagnetic Cr_2O_3,[47] and can be considered as proof of the establishment of an exchange bias. A spin glass feature as well as minor hysteresis effects, which also may introduce vertical and horizontal shifts in the magnetization loop traced after insufficient high magnetic field cooling, are not able to describe correctly the observed magnetic properties of the NiO/$CoFe_2O_4$ nanocomposite. Indeed, if the system exhibits spin glass behavior, the exchange bias does not saturate for a high cooling field but rather decreases (as the cooling field increases, the spin glass aligns increasingly with the field behaving as a ferromagnet, thus not able to pin the ferromagnet in an effective way).[48] If the system exhibits minor hysteresis, the choice of a cooling field sufficient to saturate the sample or at least be higher than the field value needed to close the loop is a minimal precaution to observe the exchange bias.[49] A cooling field as high as 70 kOe must avoid spurious results.

The observed shift of the loop along the field and magnetization axes using various cooling fields (from 15 to 70 kOe) coupled with the significant blocking temperature increases observed for the NiO/$CoFe_2O_4$ composite can be considered as a quite serious indication of the installation of the exchange bias. The interface exchange coupling between the 2.5 nm $CoFe_2O_4$ ferrimagnetic nanoparticles and their surrounding NiO antiferromagnetic shell improves the magnetic stability of these particles.

Note that the shift of the FC hysteresis loop is observed by FC from a room temperature value largely lower than the Néel temperature of NiO (525 K) but higher than the blocking temperature of $CoFe_2O_4$. In common antiferromagnetic/ferro- or ferrimagnetic structures, the shift usually is observed when the magnetic cooling field is applied at a temperature between T_N and T_C, the Néel and Curie temperatures of the antiferromagnetic and ferro- or ferrimagnetic parts of the structures, respectively.[50,51] In nanoparticles, exchange bias effects would appear when the particles are field cooled from above their blocking temperature.[47] A more systematic study on the influence of the strength of the cooling field and temperature at which it is applied must be carried out in the future for a better understanding of the observed magnetic properties of the 2.5 nm $CoFe_2O_4$ nanoparticles embedded in NiO produced by the so-called polyol process.

Conclusion

$CoFe_2O_4$ embedded in NiO nanoparticles was successfully prepared by the so-called polyol method. A nickel layered hydroxide salt was first synthesized in the presence of ferrite particles, and the calcination of the composite resulted in the formation of the desired product. The occurrence of an exchange anisotropy effect between the ferrimagnetic core and the antiferromagnetic NiO shell resulted in a shift of the FC hysteresis loops at 5 K. This effect induced a net increase in the blocking temperature when one compares the magnetic properties of $CoFe_2O_4$ dispersed in a diamagnetic matrix to that of $CoFe_2O_4$ embedded in antiferromagnetic NiO. Unfortunately, T_B remained lower than room temperature. However, optimization of the parameters, particularly of the ferrite/NiO ratio, has to be carried out. Moreover, this synthesis route is very promising since it is versatile and allows the consideration of various ferro-, ferri-, and antiferromagnetic systems.

(44) Wu, X. W.; Chien, C. L. *Phys. Rev. Lett.* **1998**, *81*, 2795.
(45) Trohidou, K. N.; Vasilakaki, M.; Del Bianco, L.; Fiorani, D.; Testa, A. M. *J. Magn. Magn. Mater.* **2007**, *316*, 82.
(46) Salazar-Alvarez, G.; Sort, J.; Suriñach, S.; Baro, M. D.; Nogués, J. *J. Am. Chem. Soc.* **2007**, *129*, 9102.
(47) Sort, J.; Langlais, V.; Doppiu, S.; Dieny, B.; Suriñach, S.; Muñoz, J. S.; Baro, M. D.; Laurent, C.; Nogues, J. *Nanotechnology* **2004**, *15*, 211.
(48) Nogués, J.; Sort, J.; langlais, V.; Skumryev, V.; Suriñach, S.; Muñoz, J. S.; Baro, M. D. *Phys. Rep.* **2005**, *422*, 65.
(49) Geshev, J. *J. Magn. Magn. Mater.* **2007**, *313*, 266.

(50) Berkowitz, A. E.; Takano, K. *J. Magn. Magn. Mater.* **1999**, *200*, 552.
(51) Kumar, P. A.; Mandal, K. *J. Appl. Phys.* **2007**, *101*, 113906.